euspen's 25th International Conference &
Exhibition, Zaragoza, ES, June 2025
www.euspen.eu

High-precision microstructure contouring coordinate measurement technology

Yufang Zhou[1, 2] , Zelong Li [1, 2,] Chaoliang Guan[1, 2] ,Yifan Dai[1, 2,] Junfeng Liu[1, 2], Wenhui Chen[1, 2], and Tao Lai [1, 2,3 ,*]

[1]*National Key Laboratory of Equipment State Sensing and Smart Support College of Intelligence Science, National University of Defense Technology, Changsha 410073, China*
[2]*Hu'nan Key Laboratory of Ultra-precision Machining Technology, Changsha 410073, China*
[3]*Hunan Institute of Advanced Technology, Changsha, Hunan, 410072, China*

Corresponding author：laitao_nudt@163.com

Abstract

This study presents a high-precision surface matching method combining an enhanced Iterative Closest Point (ICP) algorithm and Synchronous Iterative Localization (SIL) technique to address point cloud alignment accuracy and systematic error compensation in coordinate measuring machines. Key innovations include: (1) A multi-objective weighting mechanism integrating adaptive thresholds, curvature, normal vectors, and distance weighting, enhancing registration accuracy and convergence efficiency of ICP; (2) A continuous full-range sensor calibration method using low-sag spherical surfaces, overcoming limitations of traditional discrete calibration and achieving 0.1µm error compensation accuracy over a 400µm range; (3) Optical glass guideways with controlled nano-level geometric error correction, significantly reducing motion errors. Experimental results demonstrate sub-nanometer surface matching errors (＜1nm) with the improved ICP and 90% reduction in sensor linear errors. Post-compensation measurements of complex surfaces align closely with interferometer data (PV/RMS deviations <100nm), validated through high-precision 3D topography detection of fast-tool-servo-machined sinusoidal phase plates. This work establishes a novel framework for geometric error modeling and ultra-precision measurement in advanced manufacturing.

Keywords: surface matching; Iterative Closest Point; measurement machine; high-precision; microstructure measurement

1. Introduction

After establishing a single geometric error model for coordinate measuring machines (CMMs), the actual measured point cloud coordinates(x', y', z')of a workpiece can be simulated using its theoretical point cloud coordinates (x, y, z) and the error model. To accurately and efficiently obtain the error surface distribution(x, y, z_{residual}) , interpolation-based matching [1,2] is applied to align the actual point cloud with the theoretical one.

The Iterative Closest Point (ICP) algorithm is widely used for 3D geometric shape registration under known initial poses. Since Chen [3] and Besl [4] introduced ICP to point cloud matching, its computational efficiency and alignment accuracy have been significantly improved. Dr. Cheng Xu[5] from Huazhong University of Science and Technology proposed an adaptive coarse-to-fine ICP algorithm, which dynamically adjusts distance thresholds during iterations using statistical analysis. Traditional methods suffer from tedious threshold tuning and low precision, whereas ICP effectively addresses these limitations. Rusinkiewicz[6] further optimized ICP for real-time 3D reconstruction. Subsequent variants, including Go-ICP [7,8], HT-ICP [9,10], Sparse ICP [11], Generalized-ICP [12], and Multi-Channel Generalized-ICP [13], generally involve six stages: sampling, matching, weighting, rejection, error metric definition, and error minimization.

For the sampling stage, the following strategies are applied to select 10% of the points:

(a) Uniform and random sampling reduce computational complexity and enhance convergence.

(b) Normal space representation unifies normals across different orientations, aiding feature extraction.

(c) Curvature-based sampling within a Principal Component Analysis (PCA) framework [14,15] estimates curvature as the ratio of the minimum eigenvalue to the sum of eigenvalues, enabling effective surface characterization.

2. Methodology

In the objective function, distinct weights can be assigned to corresponding point pairs *p(x,y,z)* and *q(x,y,z)*, where lower weights are allocated to pairs with larger point-to-point distances. This approach mimics the rejection of pairs exceeding a distance threshold while avoiding discontinuities inherent in traditional methods. Three primary weighting strategies are defined as fellow.

(1)Compatibility-based weight:

$$w = \vec{n}_p \cdot \vec{n}_q \tag{1}$$

where n_p and n_q are denote the normal vectors of points points p and point q

(2) Normalized curvature-based weight:

$$w = e^{-(c_p - c_q)^2} \tag{2}$$

where c_p， c_q represent the curvature values of p and q , and r is the radius of curvature.

(3) Distance-weighted scheme:

$$w = 1 - \frac{dist(p,q)}{dist_{\max}} \tag{3}$$

where $dist(p,q)$ is the Euclidean distance between p and q， and $dist_{max}$ is the maximum pairwise distance in the point cloud.

For practical datasets with partial overlaps, the top 10% of point pairs with the largest distances and those near vertices/edges are filtered out. This rejection strategy enhances computational efficiency and alignment accuracy. The objective function is minimized through two error metrics:

Point-to-point minimization:

$$e = \min \sum_{i=1}^{N} \left\| \mathbf{R} q_i + \mathbf{T} - p_i \right\|^2 \tag{4}$$

Point-to-plane minimization:

$$e = \min \sum_{i=1}^{N} [(\mathbf{R} q_i + \mathbf{T} - p_i) \cdot \vec{n}_i]^2 \tag{5}$$

where *R* and *T* are the rotation and translation matrices, respectively, combined into a unified transformation matrix **g**.

The ICP algorithm aims to iteratively refine **g** to achieve precise registration between actual and ideal point clouds. Each iteration involves three steps: (1) correspondence search, (2) error metric minimization to update **g**, and (3) convergence check. This loop continues until optimal alignment is attained, as illustrated in Figure 1.

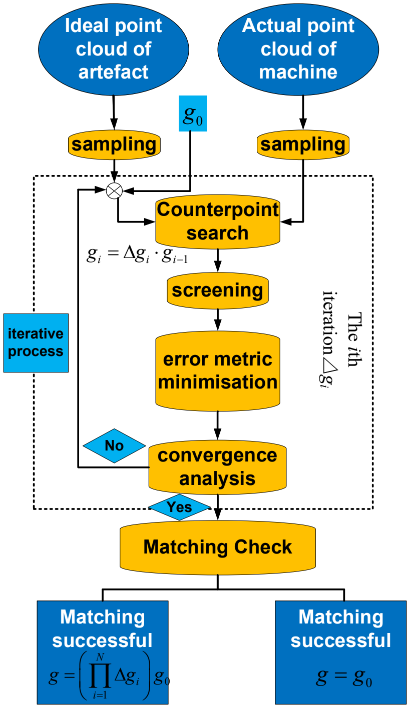

Figure 1. ICP algorithm flow

To evaluate coordinate-measured point cloud results, a surface matching technique based on the Synchronous Iterative Location (SIL) algorithm [16-18] is developed, extending the ICP framework. As illustrated in Figure 2, the key parameter is the transformation matrix **g** that maps points from the workpiece coordinate system C_M to the measuring machine coordinate system C_W.

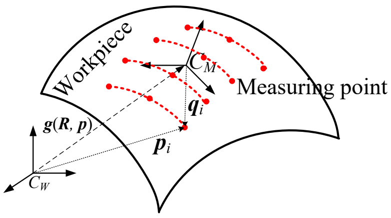

Figure 2. The corresponding relationship between the workpiece coordinate system and the measuring machine coordinate system

Let $p_i = [x_i', y_i', z_i', 1]^T$ denote a point in C_M, and $q_i = [x_i, y_i, z_i, 1]^T$, its corresponding point in C_M,. Under ideal error-free conditions, the transformation satisfies:

$$q_i = g^{-1} p_i \tag{6}$$

However, practical errors prevent direct solution of Eq. (6). To address this, a least-squares criterion is adopted to minimize the squared distance between corresponding points:

$$e(\boldsymbol{g}, Q) = \sum_{i=1}^{N} \left\| \boldsymbol{g}^{-1} \boldsymbol{p}_i - \boldsymbol{q}_i \right\|^2 \tag{7}$$

where $Q = \{q_i = \phi(u_i, v_i), i = 1, \ldots, n\}$ represents the measured point set in C_M。

The optimal transformation matrix **g** is achieved when *e* in Eq. (7) is minimized. This requires calculating the normal vector n_i along the direction $g^{-1}p_i$-q_i and determining the projected point $q_i = \phi(u_i, v_i)$ in C_W. As shown in Figure 3 the minimum squared distance is attained when the normal vector and projection point satisfy the orthogonality condition:

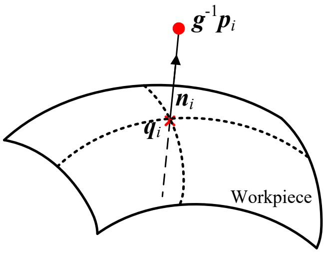

Figure 3. Matching the nearest point

$$\begin{cases} \left\langle \boldsymbol{g}^{-1}\boldsymbol{p}_i - \boldsymbol{q}_i, \ \dfrac{\partial \phi}{\partial u}(u_i, v_i) \right\rangle = 0 \\ \left\langle \boldsymbol{g}^{-1}\boldsymbol{p}_i - \boldsymbol{q}_i, \ \dfrac{\partial \phi}{\partial v}(u_i, v_i) \right\rangle = 0 \end{cases} \tag{8}$$

3. Measurement machine system

To enhance the measurement accuracy of the coordinate measuring machine, this study employs optical-grade glass for fabricating the machine's guideways, as illustrated in Figure 4. First, all guideway surfaces are processed using controlled shaping technology. Subsequently, leveraging the reflective and transmissive properties of the optical material, the machined surfaces are measured with a wavefront interferometer to evaluate flatness, parallelism, and perpendicularity. This ensures that geometric errors of the guideways are reduced to nanometer-level precision, thereby minimizing the linear and angular motion errors of the worktable. As the angular motion errors of the guideways diminish, traditional error measurement methods become inadequate due to their limited resolution. To address this, the proposed system integrates a high-precision displacement reference, achieving a linear motion accuracy of 20 nm and a probe accuracy of 20 nm.

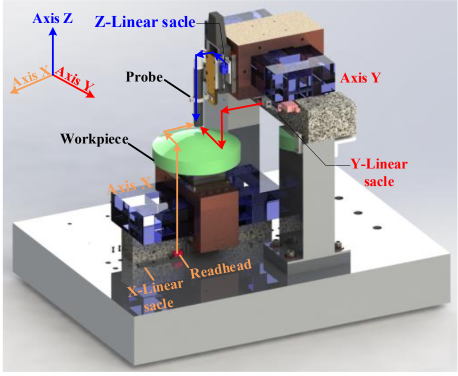

Figure 4. Profilometer measurement machine

4.Experiment

Using the proposed surface matching model, the Peak-to-Valley (PV) and Root Mean Square (RMS) values of the deviations between the measured and ideal point clouds are calculated. The surface alignment process is illustrated in Figure

5. In this figure, the measured point cloud is generated by applying translation and rotation transformations to the theoretical point cloud, implying that the measured data should theoretically exhibit zero deviation from the ideal points. However, after alignment, the residual algorithmic errors are confirmed to be below 1 nm. The computational results of this process are detailed in Figure 5, demonstrating the high precision of the proposed method.

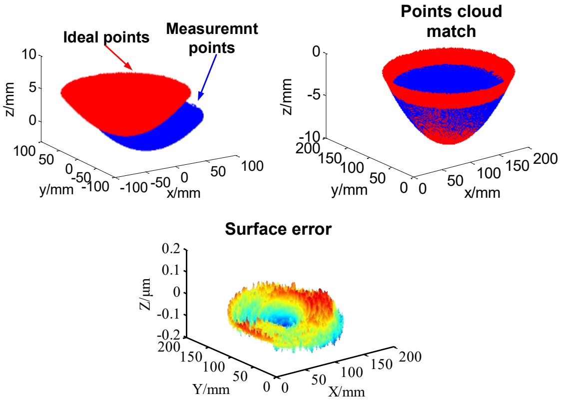

Figure 5. The actual calculation of optical complex surface shape error process

Sensor measurement error compensation involves correcting length measurement inaccuracies within the sensor's operational range (0–400 μm). According to accuracy traceability principles, the optimal approach is to calibrate the sensor using higher-precision reference devices, such as standard step gauges or laser interferometers. However, standard step gauges provide only discrete calibration points over the 0–400 μm range, failing to enable continuous calibration. While laser interferometers offer high precision, their implementation requires complex optical path alignment and rigorous measurement reference unification, resulting in cumbersome procedures.

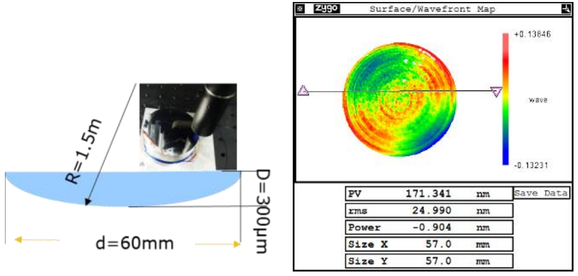

PV	171.341	nm
rms	24.990	nm
Power	-0.904	nm
Size X	57.0	mm
Size Y	57.0	mm

(a) low vector high concave spherical parameter (b) interferometer surface shape measurement results

Figure 6. Low vector height concave ball parameters

As analyzed previously, vibrations along the X and Y axes have minimal impact on measurement accuracy for low-gradient workpieces. Additionally, the 3D profilometer achieves planar measurement precision better than 100 nm within a 190 mm diameter. Leveraging these advantages, a high-precision low-sag spherical surface (sagittal height ⩽ sensor travel range) is employed for full-range sensor calibration. Smaller-aperture low-sag spheres further improve machining and calibration accuracy. A standard concave sphere with a 60 mm aperture and 300 μm sag (parameters shown in Figure 6) is utilized for calibration.

Generatrix Measurement: A generatrix of the low-sag concave spherical surface is selected for measurement. Due to the sagittal height of 300 μm (less than the sensor's 400 μm travel range), two overlapping measurements are performed:

Segment 1: 0–300 μm.

Segment 2: 100–400 μm.

The overlapping region (100–300 μm) is used to stitch the two segments into a full-range error profile.

Least-Squares Fitting: The measured generatrix profile is symmetrically split, and half is fitted using a least-squares algorithm.

Error Isolation: The fitted curve is subtracted from the measured data. Given the 30 mm aperture of the concave sphere and its low-sag geometry, influences from straightness errors and vibrations are negligible. If no sensor errors exist, residuals should be <100 nm; deviations beyond this threshold directly reflect sensor measurement errors.

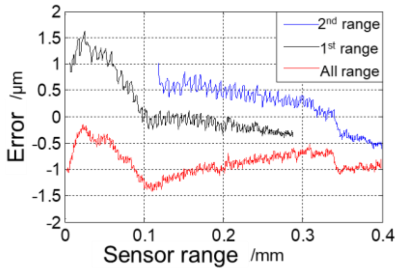

Figure 7. Measurement error of the probe

As shown in Figure 8, the probe is calibrated across different measurement ranges, with the stitched results indicated by the red line in the figure. The results reveal distinct error characteristics across the 400 μm range: the maximum error (approximately 1.2 μm) occurs in the 0–100 μm segment; a linear error relationship (≈0.9 μm) is observed between 100–350 μm; and the minimum error (≈0.1 μm) appears in the 350–400 μm range.

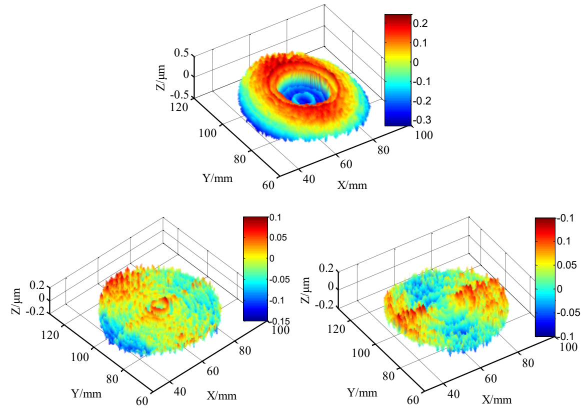

(a) Not compensated (b)compensated (c) After compensation, the workpiece is rotated by 90 ° to reproduce the measurement

Figure 8. Measurement results before and after probe error compensation

The measurement errors of a non-contact sensor are calibrated using a standard low-sag spherical generatrix to enhance measurement accuracy. After error compensation, the surface topography of the concave sphere is measured, as shown in Figure 7 Prior to compensation, sensor errors significantly degrade measurement quality, resulting in poor surface profiles. Post-compensation, the measured concave sphere profile closely matches interferometer results, with consistent height distribution. To further compare the 3D profilometer and interferometer measurements, the profilometer data is imported into ZYGO's MetroPro software for analysis.

A comparison of Figure 6(b) and 9(a) demonstrates that, after compensation, the surface profiles measured by the interferometer and the 3D profilometer exhibit high consistency, with nearly identical peak-to-valley (PV) and root mean square (RMS) errors. The pointwise difference between the two measurements is shown in Figure 9(b).

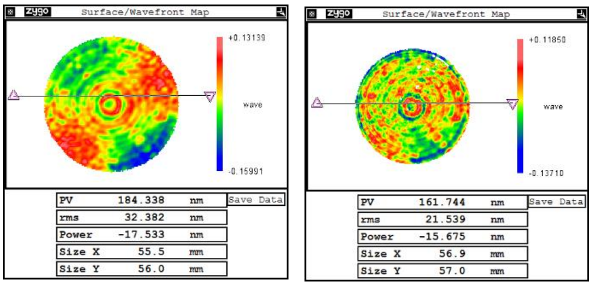

PV 184.338 nm
rms 32.382 nm
Power -17.533 nm
Size X 55.5 mm
Size Y 56.0 mm

PV 161.744 nm
rms 21.539 nm
Power -15.675 nm
Size X 56.9 mm
Size Y 57.0 mm

(a) profilometer measurement results (b)point-to-point difference results

Figure 9. The measurement results of the profilometer are compared with those of the interferometer

For the fast-tool-servo (FTS)-machined sinusoidal phase plate, measurements were conducted under the following parameters: Fast-axis stroke is 5 mm.Motion bandwidth is 20 Hz.Tracking accuracy is <2 μm.During sinusoidal array machining (50 μm amplitude, 100 μm height variation) and radial pattern machining (25 μm amplitude, 50 μm height variation), wavefront interferometers and coordinate measuring machines (CMMs) are unsuitable due to limitations in speed, flexibility, and precision. The custom-developed 3D profilometer was employed for rapid and high-accuracy measurements. As shown in Figure 10, the measured profiles yield PV values of 100.36 μm and 50.44 μm, respectively.

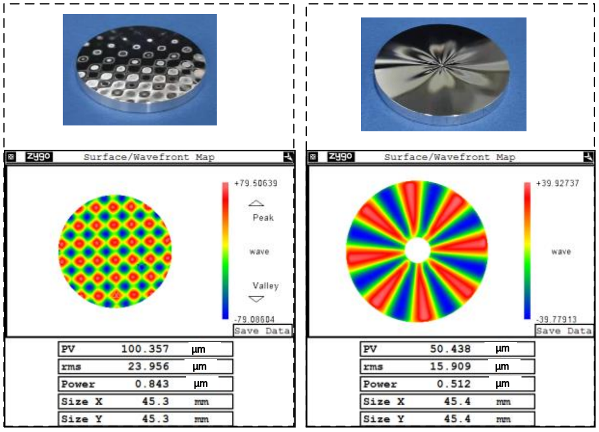

PV 100.357 μm
rms 23.956 μm
Power 0.843 μm
Size X 45.3 mm
Size Y 45.3 mm

PV 50.438 μm
rms 15.909 μm
Power 0.512 μm
Size X 45.4 mm
Size Y 45.4 mm

(a) Sinusoidal array surfaces (b) Sine radiating surface

Figure 10. Sine phase plate measurement

5. Conclusion

This study significantly enhances the accuracy and efficiency of coordinate measuring machines (CMMs) through the integration of an improved Iterative Closest Point (ICP) algorithm, Synchronous Iterative Localization (SIL)-based surface matching, and system-level error compensation strategies. Key innovations include:

Multi-weight ICP optimization: A framework combining adaptive thresholds and curvature-weighted strategies reduces matching uncertainties, enabling sub-nanometer surface error analysis.

Continuous sensor calibration: A low-sag spherical surface-based method with stitching algorithms resolves full-range error compensation, reducing sensor linear errors from 1.2 μm to 0.1 μm.

Nanoscale optical guideway correction: Achieves angular motion error identification beyond traditional limits.

Experimental validation confirms post-compensation complex surface measurements exhibit PV/RMS deviations <100 nm compared to interferometer results, while fast-tool-servo-machined phase plates achieve micrometer-level contour detection accuracy. This methodology provides a reliable technical foundation for efficient inspection of high-gradient optical components and microstructured surfaces, demonstrating significant engineering value.

References

[1] Huang Z, Wen Y, Wang Z, et al. Surface reconstruction from point clouds: A survey and a benchmark[J]. IEEE transactions on pattern analysis and machine intelligence, 2024.

[2] Bao J, Yuan X, Huang G, et al. Point Cloud Plane Segmentation-Based Robust Image Matching for Camera Pose Estimation[J]. Remote Sensing, 2023, 15(2): 497.

[3] Chen Y, Medioni G. Object modeling by registration o fmultiple range images[C]. Proceedings of the IEEE International conference on robotics and automation sacramento.1991, 2724-2729.

[4] Besl P, Mckay N. A method for registration of 3D shapes[J]. Proceedings fo SPIE-The international society for optical engineering, 1992, 14(3): 239~256.

[5] Cheng Xu. Research on 3D reconstruction and point cloud registration technology of complex parts [D]. Wuhan: Huazhong University of Science and Technology, 2019, 86 ~ 99.

[6] Rusinkiewicz. S, Hall-Holt O, Levoy M. Real-time 3D model acqusition[J]. ACM transactions on graphics(TOG), 2002, 21(3):438~446.

[7] Kolpakov A, Werman M. An approach to robust ICP initialization[J]. IEEE Transactions on Pattern Analysis and Machine Intelligence, 2023, 45(10): 12685-12691.

[8] Denayer M, De Winter J, Bernardes E, et al. Comparison of point cloud registration techniques on scanned physical objects[J]. Sensors, 2024, 24(7): 2142.

[9] You B, Sun M, Li J. High-accuracy pose estimation algorithm with monocular camera based on residual network[J]. Optical Engineering, 2023, 62(5): 054102-054102.

[10] Kang C, Geng C, Lin Z, et al. Point cloud registration method based on geometric constraint and transformation evaluation[J]. Sensors, 2024, 24(6): 1853.

[11] Bouaziz S, Tagliasacchi A, Pauly M. Sparse iterative closest point[C]. Computer graphics forum. Blackwell Publishing Ltd, 2013, 32(5): 113~123.

[12] Koukoulis E, Arvanitis G, Moustakas K. Unleashing the Power of Generalized Iterative Closest Point for Swift and Effective Point Cloud Registration[C]//2024 IEEE International Conference on Image Processing (ICIP). IEEE, 2024: 3403-3409.

[13] Servos J, Waslander S L. Multi-Channel Generalized-ICP: A robust framework for multi-channel scan registration[J]. Robotics and Autonomous Systems, 2017, 87: 247~257.

[14] Jolliffe I T. Principal component analysis[J]. Journal of Marketing Research, 2002, 87(4):513.

[15] Greenacre M, Groenen P J F, Hastie T, et al. Principal component analysis[J]. Nature Reviews Methods Primers, 2022, 2(1): 100.

[16] Peng X, Yang C, Hao H, et al. Measurement and algorithm for localization of aspheric lens in magnetorheological finishing[J]. International Journal of Advanced Manufacturing Technology, 2017, 88(9-12):1~9.

[17] Yang Can. Workpiece self-positioning algorithm and system implementation in magnetorheological finishing [D]. Changsha: National University of Defense Technology, 2015, 9-21.

[18] Meng Y, You Z, Wang X, et al. An atomic force microscope-like dual-stage force controlled fast tool servo for in-process inspection of micro-structured surfaces[J]. Mechanical Systems and Signal Processing, 2024, 219: 111605.